


Cation segregation observed in an $(\text{In,Ga})_2\text{O}_3$ material thin film library beyond the miscibility limit of the bixbyite structure

S. Montag , D. Splith, M. Kneiß, and M. Grundmann


Felix-Bloch-Institut für Festkörperphysik, Fakultät für Physik und Geowissenschaften, Universität Leipzig, Linnestraße 5, 04103 Leipzig, Germany

J. Garcia Fernandez * and Ø. Prytz 

Department of Physics/Centre for Materials Science and Nanotechnology, University of Oslo, P.O. Box 1048 Blindern, N-0316 Oslo, Norway

H. von Wenckstern †

Felix-Bloch-Institut für Festkörperphysik, Fakultät für Physik und Geowissenschaften, Universität Leipzig, Linnestraße 5, 04103 Leipzig, Germany
and Department of Physics/Centre for Materials Science and Nanotechnology, University of Oslo, P.O. Box 1048 Blindern, N-0316 Oslo, Norway

 (Received 17 May 2023; revised 29 August 2023; accepted 30 August 2023; published 26 September 2023)

Structural, morphological, and optical properties of $(\text{In}_{1-x}\text{Ga}_x)_2\text{O}_3$ thin films are reported as a function of the cation composition. A material library with $0.1 \leq x \leq 0.64$ was fabricated by discrete combinatorial synthesis on *r*-plane sapphire substrates using pulsed laser deposition. The samples crystallize in the cubic bixbyite phase for $x \leq 0.35$. The lattice constant and absorption edge energy systematically decrease and increase, respectively, with increasing Ga content up to $x = 0.2$. For higher Ga admixtures, both saturate. In addition, a significant change in surface morphology occurs at $x \sim 0.2$. Transmission electron microscopy examinations of selected samples show a homogeneous incorporation of Ga_2O_3 into cubic In_2O_3 for $x = 0.11$, while a segregation of Ga-rich and In-rich regions can be seen for $x = 0.22$ and $x = 0.35$. In the sample with $x = 0.35$, the Ga-rich regions exhibit a preferred orientation with an angle of 45° – 55° with respect to the substrate normal, which has been shown to result from a correspondingly faceted In-rich bixbyite layer at the substrate–thin film interface.

DOI: [10.1103/PhysRevMaterials.7.094603](https://doi.org/10.1103/PhysRevMaterials.7.094603)

I. INTRODUCTION

Combinatorial thin film synthesis significantly accelerated the discovery of novel materials over the past two decades. The first thin film material libraries were already created in the 1960s by physical vapor deposition methods using coevaporation of metals by Kennedy *et al.* [1], simultaneous sputtering (cosputtering) of Au and SiO_2 by Miller and Shirn [2], or sputtering of segmented ceramic targets by Hanak and Gittleman [3]. Since then, numerous synthesis and characterization methods have been adapted to generate material libraries and screen their physical properties [4,5]. A recent, novel segmented target approach, adopted in 2013 to the requirements of pulsed laser deposition (PLD) [6], enables discrete composition combinatorial thin film synthesis [7,8], continuous composition spread thin films [6,8], as well as the creation of compositional gradients in growth direction, e.g., for strain engineering [7,8]. This combinatorial PLD (C-PLD) method was used, for instance, to grow and characterize physical properties of material libraries of group-III sesquioxide alloys [9–32], of which gallium oxide has attracted tremendous

scientific and technological interest due to its promising material properties for high-power electronics [33–36]. Each of the group-III sesquioxides crystallizes in various polymorphs. For Ga_2O_3 , the thermodynamically stable phase is the monoclinic β -gallia structure, and metastable phases are the orthorhombic κ , the rhombohedral α , and the cubic spinel γ phases [37]. Indium oxide crystallizes in the stable cubic bixbyite phase ($\text{c-In}_2\text{O}_3$) or the metastable rhombohedral phase [34]. It is well suited as a highly conductive transparent electrode [38], and tin-doped indium oxide (known as ITO) is used commercially in photovoltaic modules, displays, touch panels, etc. It also has potential as a transparent semiconductor due to its high electron mobility. So far, the literature on active, crystalline In_2O_3 -based semiconducting devices is limited to *pn* diodes [39], Schottky barrier diodes [40], and gas sensors [41,42]. Further, only few publications on band-gap engineering of indium oxide by isovalent substitution are available. Early work by Cava *et al.* focused on transparent conducting oxide applications of monoclinic InGaO_3 layers doped by Sn or Ge [43]. Edwards *et al.* prepared ceramic solid solutions of In_2O_3 and Ga_2O_3 and provided structural properties of cubic bixbyite $(\text{In}_{1-x}\text{Ga}_x)_2\text{O}_3$ and a phase diagram with miscibility gap for $x > 0.07$ [44]. Ceramic $(\text{In}_{1-x}\text{Ga}_x)_2\text{O}_3$ pellets, investigated by Regoutz *et al.*, had the solubility limit slightly lower at $x \sim 0.06$ [45]. For thin films grown by metal-organic

*j.g.fernandez@smn.uio.no

†wenckst@uni-leipzig.de, holgervw@uio.no

vapor phase deposition on (00.1)Al₂O₃ or (100)ZrO₂, a much larger amount of Ga in cubic (In_{1-x}Ga_x)₂O₃ with $x \leq 0.5$ was reported by Yang *et al.* [46] and Kong *et al.* [47], respectively, but a systematic dependence of the lattice parameter on the Ga content and thus evidence for the inclusion of Ga_{In} was not provided. Zhang *et al.* prepared cubic (In_{1-x}Ga_x)₂O₃ thin films by PLD on (00.1)Al₂O₃ with $x = 0.17$ and 0.44 [48]. The room temperature absorption edge of both layers was slightly higher than 4 eV.

Swallow *et al.* investigated electronic and optical properties by x-ray photon spectroscopy (XPS) and transmission measurements of a spatially addressable (In, Ga)₂O₃ thin film material library, grown by C-PLD, consisting of regions with monoclinic and cubic phase for Ga- and In-rich parts, respectively [27]. For the cubic phase, a downward surface band bending accompanied by electron accumulation was observed, reversing at the phase transition to the monoclinic polymorph occurring at $x \sim 0.31$ [27]. The absorption edge systematically increases with increasing Ga content across the entire library and was modeled by $E_g(x) = E_{\text{abs,Ga}_2\text{O}_3}x + E_{\text{abs,In}_2\text{O}_3}(1-x) - b \times x(1-x)$ with values $E_{\text{abs,Ga}_2\text{O}_3} = 4.71$ eV, $E_{\text{abs,In}_2\text{O}_3} = 3.72$ eV, and $b = 0.36$ eV [27]. In a similar continuous composition spread (CCS) thin film material library, the metastable hexagonal InGaO₃ phase (space group *P6/mmc*) was revealed for $x \approx 0.5$ [21]. This phase has previously only been reported for high-pressure synthesis [49]. It is made up of alternating In-O and Ga-O layers stacked along the *c* direction where Ga and In are bonded to five or six oxygen anions, respectively. Another XPS study of a spatially addressable material library was published by Nagata *et al.* and confirmed the downward band bending for lower Ga contents ($x \leq 0.4$). A recent XPS investigation of laterally homogeneous (In, Ga)₂O₃ thin films prepared by standard PLD using various differently composed (In, Ga)₂O₃ targets by Yang *et al.* [50] confirmed the trends observed in the material libraries of Swallow *et al.* and Nagata *et al.* Structural, optical, and phonon mode properties of cubic, single-crystalline (In, Ga)₂O₃ thin films grown by molecular beam epitaxy on a binary In₂O₃ buffer layer on yttria-stabilized zirconia were recently published by Feldl *et al.* and Papadogianni *et al.* [51,52]. The binary buffer layer, grown at reduced temperature, is necessary to improve the initial wetting of the substrate and to reduce void formation at the interface to the yttria-stabilized zirconia (YSZ) substrate. This buffer layer induces strain at the interface to the subsequently deposited (In, Ga)₂O₃ layers. From x-ray diffraction measurements, the lattice constant was determined to decrease according to Vegard's law up to the highest investigated Ga content of $x = 0.18$. However, Raman measurements and spectroscopic ellipsometry reveal a saturation of phonon mode frequencies and the optical absorption edge for $x \geq 0.08$, respectively. Microstructural analysis by transmission electron microscopy and electron-dispersive x-ray spectroscopy showed that for $x > 0.11$ Ga-rich regions with Ga cation share up to 50% are incorporated. Interestingly, the bixbyite phase was maintained in these regions; however, the amount of oxygen was reported below its stoichiometric value [52]. Cation segregation in group-III sesquioxides has also been reported for a highly strained β -(Al_{0.48}Ga_{0.52})₂O₃ layer grown by

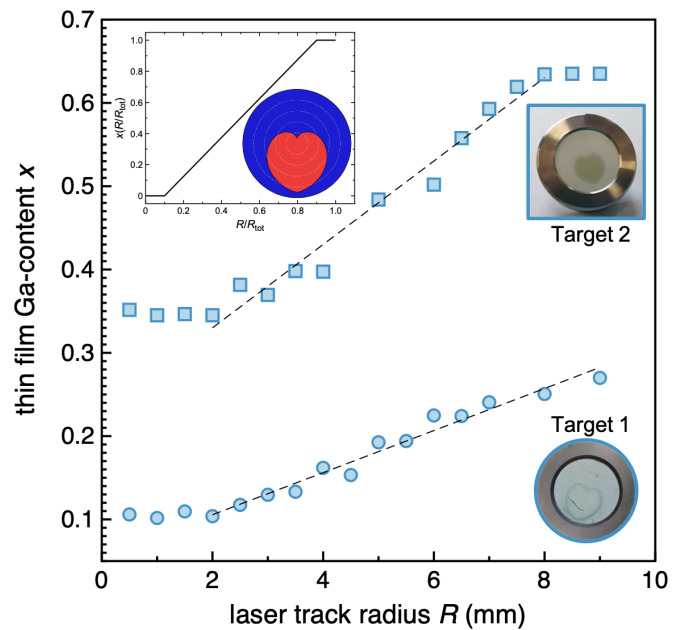


FIG. 1. Dependence of Ga content, determined by EDXS, on the radius R of the laser track T for Targets 1 and 2, as illustrated by photographic images. The dashed lines are linear fits. The inset depicts the expected linear composition variation [8] due to path length difference of T with radius R (white dashed lines) in the inner and outer segments with $x = 0$ and $x = 1$, respectively.

metal-organic chemical-vapor deposition on binary β -Ga₂O₃. There are numerous reports of cation accumulation on group-III sesquioxide surfaces. Whether cation segregation can occur in the bulk of fully relaxed thin films unstrained by buffer or nucleation layers, or within a heterostructure, has not been investigated and would facilitate understanding of its origin and potential exploitation in functional layers or devices.

Overall, available results on cubic (In, Ga)₂O₃ are not yet fully consistent. We fabricated a material library of (In_{1-x}Ga_x)₂O₃ thin films on *r*-plane sapphire substrates (without buffer layer) with selected compositions up to $x = 0.64$ by C-PLD. We discuss miscibility, phase limits, and saturation of physical properties for higher Ga content and present information gained from microstructural analysis. We do not observe reflections in x-ray diffraction (XRD) connected to the monoclinic β -gallia phase in the investigated composition range; however, a systematic decrease (increase) of the *c*-lattice constant (absorption edge) is observed for $x \leq 0.2$. In agreement with the work of Papadogianni *et al.*, we identify Ga-rich regions in samples with higher Ga content; here for $x \geq 0.22$. These regions show a regular arrangement within a polycrystalline In₂O₃ matrix clearly evident in a sample with $x \sim 0.35$.

II. EXPERIMENT

(In_{1-x}Ga_x)₂O₃ thin films on *r*-plane sapphire substrates were grown by pulsed laser deposition using two radially segmented PLD targets with a heart-shaped inner segment (corresponding to two joined Archimidean spirals with a rotational angle $\leq \pi$; cf. insets of Fig. 1) enabling a tailored variation of the time-averaged material flux composition

that depends linearly on the radius of the laser track [8]. All samples were grown at a substrate temperature of about 500 °C and an oxygen pressure of 0.02 mbar without initial growth of wetting or buffer layers. The target to substrate distance was 9 cm. The targets were fabricated in house. Commercial source powders (Alfa Aesar) were placed in positions predefined by a form with a heart-shaped inner segment. After removal of the form, targets were pressed and finally sintered at 1350 °C for 72 h in ambient atmosphere. The composition of the segments of the targets were as follows: for the Target 1 inner (outer) segment: In_2O_3 [$(\text{In}_{0.7}\text{Ga}_{0.3})_2\text{O}_3$]; and for the Target 2 inner (outer) segment: $(\text{In}_{0.7}\text{Ga}_{0.3})_2\text{O}_3$ [$(\text{In}_{0.4}\text{Ga}_{0.6})_2\text{O}_3$]. The chemical composition of the thin films was determined by energy-dispersive x-ray spectroscopy (EDXS) using a Nova NanoLab 200 by FEI Company equipped with a Bruker Quantax 200 detector. XRD measurements were acquired using a PANalytical X'pert PRO MRD diffractometer, equipped with a PIXcel3D detector, operating in one-dimensional line scanning mode with 255 channels. Optical absorption was measured using a UV/VIS dual beam spectrometer Lambda 19 from Perkin-Elmer. The optical band-gap energy $E_{g,\text{opt}}$ and the layer thickness d were obtained from the transmission spectra of the samples by extrapolation of $(\alpha h\nu)^2$ vs photon energy to zero and by evaluation of the layer thickness oscillations using a refractive index of $n = 2$, respectively. The surface properties were determined employing a Park Systems XE-150 atomic force microscope (AFM) in noncontact mode.

Cross-sectional transmission electron microscopy (TEM) samples were prepared by mechanical grinding, polishing, and final thinning by Ar ion milling in a Gatan PIPS II (Model 695). Plasma cleaning (Fishione Model 1020) was performed immediately before the TEM investigations. A JEOL JEM-2100F microscope operated at an acceleration voltage of 200 kV was used for high-resolution transmission electron microscopy (HRTEM) investigations. Scanning TEM (STEM) imaging and EDXS measurements were done at 300 kV in a Cs-corrected Thermo Fisher Scientific Titan G2 60-300 kV microscope equipped with Super-X EDXS detectors and a Quantum GIF. The STEM images were recorded using a probe convergence semiangle of 23 mrad, a nominal camera length of 60 mm using two different detectors: high-angle annular dark field (HAADF; collection angles 100–200 mrad) and bright field (BF; collection angles 0–22 mrad). In the HAADF image, the location of the indium cations is clearly visible as the brighter contrast (atomic number $Z = 49$), while the darker contrast is associated with gallium cations (atomic number $Z = 31$). Simulated HRTEM images were calculated using the RECI PRO software package [53].

III. CREATION OF DISCRETE COMPOSITION SPREAD MATERIAL LIBRARY

The ablation of radially segmented PLD targets allows one to adjust the time-averaged material flux incident on a substrate by controlling the radius R of the laser track T [7,8]. The path length of T in the outer segment increases with increasing R and with that the time-averaged Ga content of the ablated material for the targets used in this study. This enables the growth of sets of homogeneous thin films (R is fixed during

the deposition of a specific sample) with a well-defined and systematic change of chemical composition (representing a discrete composition spread material library) and it requires a significantly lower number of targets compared to conventional PLD. In the insets of Fig. 1 photographic images of the two targets used in this study are depicted. The composition range, covered in our material library, ranges from $x = 0.1$ to $x = 0.64$. For that, the laser track radius R was varied in steps of 0.5 mm between 1 and 9 mm for each target. The resulting variation of the Ga content in the deposited thin films is shown in Fig. 1. For small radii $R \leq 2$ mm the laser track is only within the inner target segment and the thin film composition is independent of R . For both targets, the thin film composition is higher than the Ga content of the inner segment in this range of R . For $R \geq 8$ mm, the Ga content saturates only for Target 2, since its inner segment is slightly smaller than for Target 1 (cf. images of segmented targets in Fig. 1). Otherwise the Ga content in the thin films increases linearly for both targets as indicated by the linear fits and as expected from the linear change of the path length ratio with R [8].

IV. RESULTS AND DISCUSSION

The structural thin film properties were investigated by XRD. Figure 2 depicts 2θ - ω diffractograms for selected samples of the material library. As reported for binary In_2O_3 on r -plane sapphire [54,55] our thin films contain domains with (111) and (110) orientation, respectively, for Ga contents $x < 0.35$ and $x > 0.56$, otherwise the intensity of the corresponding reflections is weak or within the noise level. Initially, the (222) and (444) reflections systematically shift to higher angles, indicating a decrease of the corresponding lattice plane spacing, and broaden (see Fig. 1 in [56]) with increasing Ga content. Assuming fully relaxed growth, the a -lattice constant was determined by evaluation of peak positions of the (222) and (444) reflections (not shown; for the (110)-oriented crystals only the (440) reflection had sufficient intensity). The dependence of a on the Ga content is depicted in Fig. 3 together with the data available in literature.

The linearly decreasing lattice constant can be fitted according to Vegard's law: $a(x) = a(0) + (1-x)a(1)$ with $a(0) = 10.119$ Å and $a(1) = 9.043$ Å up to Ga contents of $x = 0.19$. It correlates with the variation derived by Peelaers *et al.* [57] using first-principles calculations. The extrapolation to low Ga contents matches the experimental data of Regoutz *et al.* [45] determined for ceramic bulk samples. For fully relaxed $(\text{In}_{1-x}\text{Ga}_x)_2\text{O}_3$ on a low-temperature In_2O_3 buffer on (111)-oriented YSZ substrates, a linear decrease of the lattice constant was observed for $x \leq 0.18$ [52]. The lattice constants for a given x are slightly higher than reported here.

XRD ϕ scans for the (222) reflex of $(\text{In}, \text{Ga})_2\text{O}_3$ and the (11.3) reflex of the sapphire substrate (see Fig. 2 in [56]) reveal two reflex pairs for the $(\text{In}, \text{Ga})_2\text{O}_3$ thin films, each with a separation of 180°. The angle between adjacent reflexes of these pairs is about 86.8° representing distinct rotational domains already described by Vogt *et al.* [55] for molecular beam epitaxy grown In_2O_3 , $\text{In}_2\text{O}_3:\text{Sn}$, and $\text{In}_2\text{O}_3:\text{Mg}$ or by Schmidt *et al.* [54] for PLD grown In_2O_3 and $\text{In}_2\text{O}_3:\text{Mg}$ thin films on the r -plane sapphire. AFM images are depicted for selected compositions in Fig. 4. For low Ga content the

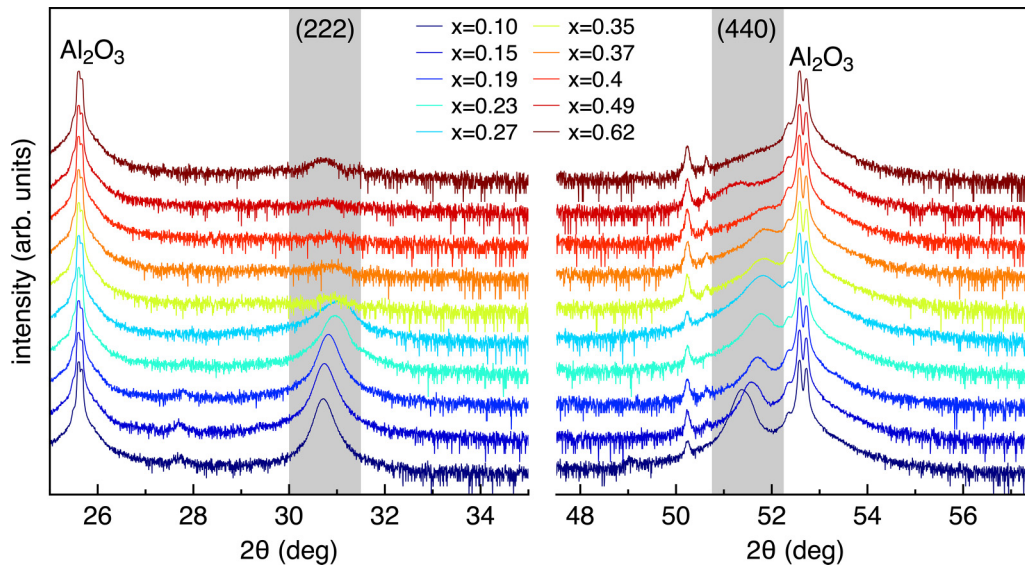


FIG. 2. 2θ - ω diffractograms of selected samples of the material library with Ga content as labeled.

two rotational domains, revealed in the XRD ϕ scans, are recognizable, which is not the case for $x \geq 0.19$. In addition, for $x > 0.19$, smaller grains appear and an assignment of the two domains is no longer possible. The change of surface morphology occurs for the same Ga content for which the a -lattice constant becomes independent of x (see Fig. 3 in [56]).

To summarize the structural investigations, the incorporation of Ga into cubic indium oxide grown on r -plane sapphire leads to a systematic and linear decrease of the a -lattice parameter according to Vegard's law (similar to the results of ceramic samples) up to $x = 0.19$. The (111) and (110) out-of-plane orientations and two in-plane rotational domains [for the (111)-oriented grains] are observed in agreement with

binary PLD grown c - In_2O_3 layers on r -plane sapphire [54]. For $x > 0.19$, the decrease of a vanishes, the grain sizes decrease strongly, and the intensity of the XRD (222) reflection reduces to a principle negligible intensity for $x \geq 0.35$.

Transmission and reflection measurements were carried out at room temperature (see Fig. 4 in [56]) to determine the shift of the absorption edge $E_{g,\text{opt}}$ as a function of the Ga content. For selected samples of the material library, the absorption coefficient is shown in Fig. 5 as a function of photon energy. The derived values of $E_{g,\text{opt}}$ are shown in Fig. 6 together with data compiled from literature. We note that there is considerable variation in the published values of $E_{g,\text{opt}}$ and that additional experimental results are needed to consolidate the trend described below. In general, the optical band gap initially increases with x but saturates for higher Ga contents limiting the range for band-gap (or better absorption edge) tuning from 3.75 eV to about 3.92 eV. The figure further depicts a linear fit to our current data according to $E_{g,\text{opt}}(x) = 3.75 \text{ eV} + 0.517 \text{ eV} \times x$ as well as the dependence of the absorption edge published by Swallow *et al.* [27]. We note that the extrapolation of the linear fit to our current data to $x = 0$ coincides with the optical band gap of binary In_2O_3 determined by Weiher and Ley [58]. Consistent with the results discussed above, the absorption edge of our sample set saturates for $x > 0.2$, demonstrating substitutional incorporation of Ga into the In_2O_3 matrix up to $x = 0.2$.

A detailed microstructural and chemical study of the samples with Ga content of $x = 0.11$, 0.22, and 0.35 was assessed by HRTEM, STEM-EDXS, and electron-energy-loss spectroscopy (EELS). Figures 7(a) and 7(b) show the corresponding low magnification HAADF and BF image of the $x = 0.11$ Ga-content sample with a quite homogeneous contrast, which suggests that there is no phase separation or heterogeneous distribution of the cations. In the corresponding BF image in Fig. 7(b), moreover, it can be seen that the sample is mainly formed by large columnar grains, with a length of 150–300 nm and a width of 30–70 nm, with slight off-orientations with respect to each other. Figure 7(c) shows the STEM-EDXS map for the same region using the $\text{In } L\alpha$

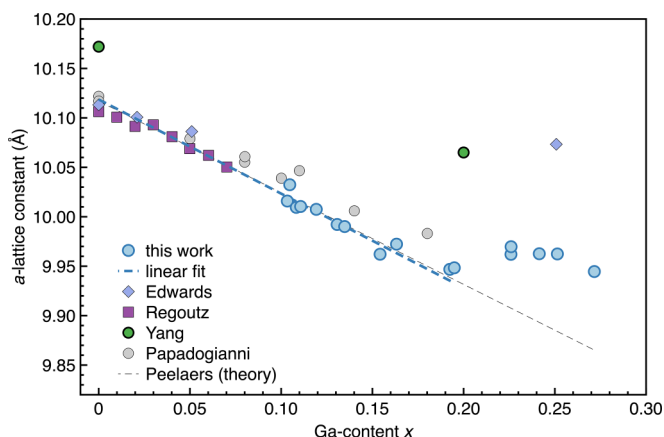


FIG. 3. a -lattice constant as a function of the Ga content of $(\text{Ga}_x\text{In}_{1-x})_2\text{O}_3$ thin films of this study and literature data of Edwards and Mason (ceramic samples) [44], Regoutz *et al.* (ceramic samples) [45], Papadogianni *et al.* (epitaxial thin films) [52], and Yang *et al.* (epitaxial thin films) [50]. The black-dashed line indicates calculated data from Peelaers *et al.* [57]. The blue-dashed line is based on a linear fit to the data of this work: $a(x) = 10.119 \text{ \AA} - (0.9524 \times x) \text{ \AA}$ and resulting in a cubic lattice constant for Ga_2O_3 of $a = 9.043 \text{ \AA}$.

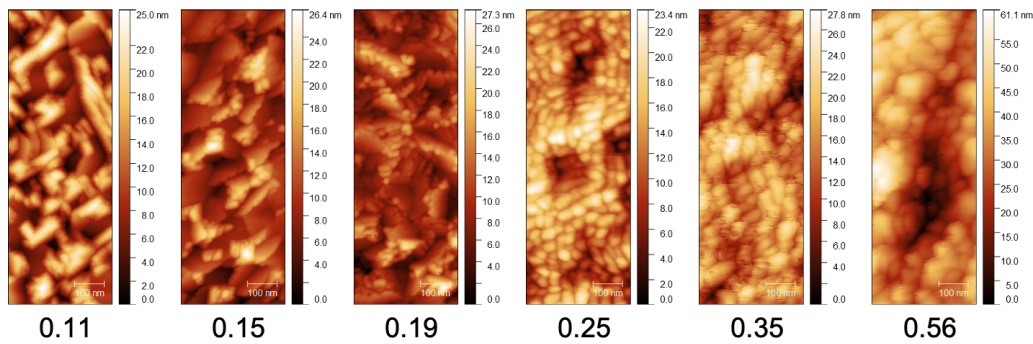


FIG. 4. Atomic force microscopy images of selected thin films with Ga content x as labeled.

and the Ga $K\alpha$ line, respectively. From the map, it can be noticed that both, In (red) and Ga (green), are homogeneously distributed. Figures 7(d) and 7(e) show two representative HRTEM images and their corresponding fast Fourier transform (FFT). Figure 7(d) corresponds to an $(\text{In}, \text{Ga})_2\text{O}_3$ grain indexed according to the bixbyite cubic phase (space group $Ia\bar{3}$ [59]) along the zone axes [112]. Furthermore, the image in Fig. 7(e) shows the boundary between two crystals corresponding to $c\text{-(In, Ga)}_2\text{O}_3$ along the zone axis [534] (top) and [110] (bottom). All this information confirms that this sample is formed only by columnar grains of $c\text{-(In, Ga)}_2\text{O}_3$ crystals, in agreement with the XRD data shown before.

Continuing with the second sample, with a Ga content of $x = 0.22$, Figs. 5(a)–5(d) in the Supplemental Material [56] show the corresponding low-magnification HAADF and BF images, together with a chemical EDXS map of a region of the sample using the In $L\alpha$ and Ga $K\alpha$ lines. From the HAADF image, two different regions can be observed in this sample: on the one hand, areas where the distribution of In and Ga is homogeneous without change in contrast, but on the other hand, also other areas with bright and dark stripes can be observed, suggesting a possible segregation of the elements. This feature is confirmed by the EDXS chemical map [see Fig. 5(b) in [56]] for In (red) and Ga (green) and the magnified EDXS map of the area showing cation segregation in regions corresponding to the stripes [see Fig. 5(c) in [56]]. As can be observed, both Ga and In are found to be segregated forming stripes of about $50 \text{ nm} \times 10 \text{ nm}$. We do

not detect any variation of the oxygen content, indicating that the stripes are formed by $c\text{-(In, Ga)}_2\text{O}_3$ (red) and gallium-rich regions (green). This result is in agreement with previous work suggesting that the solubility limit of Ga into $c\text{-In}_2\text{O}_3$ is between $x = 0.06$ [45] and $x = 0.14$ [52]. The changes in the microstructure and distribution of In and Ga of the $x = 0.22$ Ga-content sample are therefore likely connected to the saturation of the lattice constant and optical absorption edge as discussed above and shown in Figs. 3 and 6. Moreover, from the BF image [see Fig. 5(d) in [56]], it can be noticed that the grains in this sample are smaller in agreement with the AFM measurements of Fig. 4 and not as perfectly vertically oriented as in the previous sample, showing sometimes a slight tilt.

Finally, the same study has been carried out on the sample with $x = 0.35$. Figures 8(a) and 8(b) show the HAADF and BF images for this sample, respectively. As can be seen, this sample has a thickness of 450 nm, and it can be observed that the sample is made up of large bright and dark stripes stacked alternately forming an angle of $45^\circ\text{--}55^\circ$ with respect to the surface normal. Figure 8(c) depicts a high-magnification STEM HAADF image of one Ga-rich grain (dark contrast) between two $c\text{-(In, Ga)}_2\text{O}_3$ grains (bright contrast) without a crystallographic relationship between them, confirming the

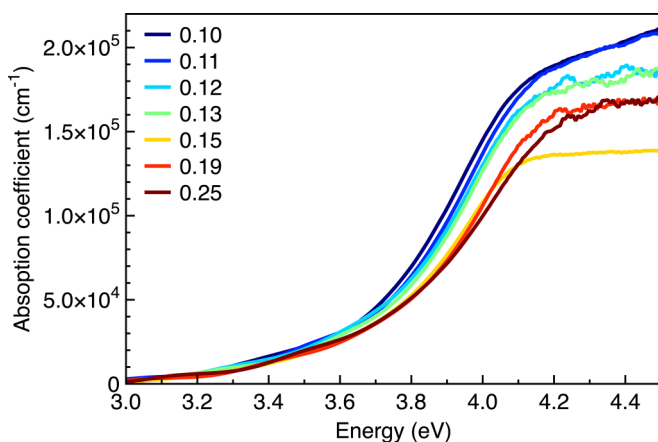


FIG. 5. Energy dependence of the absorption coefficient of selected $(\text{In}_{1-x}\text{Ga}_x)_2\text{O}_3$ thin films with Ga content x as labeled.

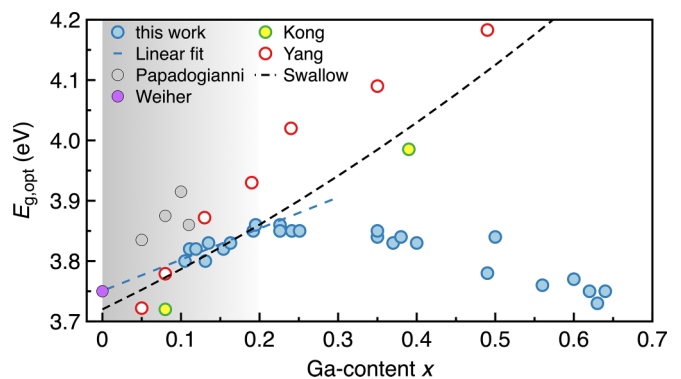


FIG. 6. Optical band gap versus Ga content of $(\text{Ga}_x\text{In}_{1-x})_2\text{O}_3$ thin films of this study and the literature data of Yang *et al.* [46], Kong *et al.* [47], and Papadogianni *et al.* [52]. Further, the data of binary In_2O_3 of Weiher and Ley [58] is included. The black-dashed line represents the band-gap dependence of Swallow *et al.* [27] (see Introduction). The blue-dashed line is a linear fit to the current data for Ga content up to 0.2: $E_{g,\text{opt}}(x) = 3.75 \text{ eV} + 0.517 \text{ eV} \times x$. The gray shaded area indicates the miscibility range for the samples in the current study.

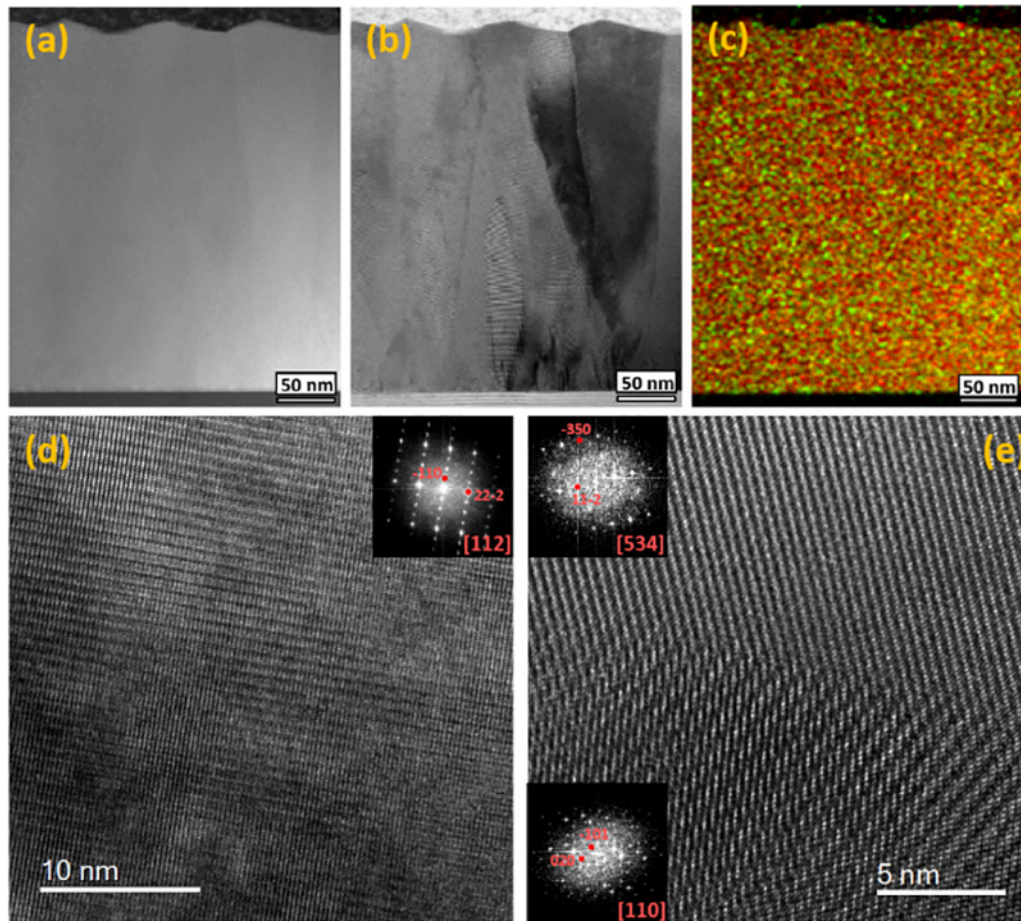


FIG. 7. Low-magnification STEM (a) HAADF and (b) BF images of the sample with $x = 0.11$. (c) STEM-EDXS map for In $L\alpha$ (red) and Ga $K\alpha$ (green) showing a homogeneous distribution of both elements. (d) and (e) HRTEM images and corresponding FFT of the columnar cubic $(\text{In, Ga})_2\text{O}_3$ crystals. The total film thickness is around 360 nm.

polycrystalline nature of the sample. Interestingly, a closer look at the area near the substrate [Fig. 8(d)] reveals that a 10-nm-thick $c\text{-(In, Ga)}_2\text{O}_3$ layer (marked in red) tends to form in first place, and after this, triangular-shaped gallium-rich crystals are stabilized (marked in green). As the film continues to grow, it forms stacks of crystals following the angles mentioned above. The EDXS spectra [Figs. 8(e) and 8(f)] confirm the presence of In and Ga in the stripes emphasizing the phenomena seen for the sample with $x = 0.22$. The stripes range in length from 50 to 300 nm for both and have a width of about 40 nm for the $c\text{-(In, Ga)}_2\text{O}_3$ (red) and 10–15 nm for the Ga-rich ones (green). The cationic percentage obtained from the EDXS profile across the yellow line in Fig. 8(f) is depicted in Fig. 8(g). We can detect the variation from $c\text{-(In, Ga)}_2\text{O}_3$ grains (around 15%–20% of Ga) to In-doped Ga-rich grains (around 40% of In). Please note that the sample is not fully homogeneous in the direction along the electron beam, so these values are only indicative of the composition of the sample.

Simultaneously, we have analyzed this sample by HRTEM. Figures 6(a)–6(c) in the Supplemental Material [56] show three representative HRTEM images and corresponding FFT of $c\text{-(In, Ga)}_2\text{O}_3$ grains together with Ga-rich grains oriented along different zone axes (the boundaries between the different phases have been marked with dashed red-green lines for better visualization). The indexation of the FFT enabled us

to identify that the $c\text{-(In, Ga)}_2\text{O}_3$ regions correspond to the bixbyite cubic structure [59]. On the other hand, the spots observed in the corresponding FFT for the Ga-rich regions, unlike those of $c\text{-(In, Ga)}_2\text{O}_3$, are weak and very diffuse. This makes it more challenging to index accurately, but the observed distances and angles are consistent both with the hexagonal phase, $h\text{-InGaO}_3$ [49], and with the β -polymorph, $\beta\text{-Ga}_2\text{O}_3$ [60]. However, the contrast observed [see Fig. 6(b) in [56]] for the gallium-rich crystal is very similar to the identified $h\text{-InGaO}_3$ previously observed by Wouters *et al.* [61]. Our HRTEM simulation of the $h\text{-InGaO}_3$ phase along the $[2\bar{1}\bar{1}0]$ zone axis corresponds very well to the experimental result for $\Delta t = 25$ nm and $\Delta f = -10$ nm [see inset of Fig. 6(c) in [56]]. Moreover, we have carried out an analysis of the In $M_{4,5}$ and O K lines of the sample by STEM-EELS [see Fig. 6(d) in [56]] over a $c\text{-(In, Ga)}_2\text{O}_3$ grain (bright contrast) and Ga-rich area (dark contrast) in the HAADF image. The spectrum recorded from a $c\text{-(In, Ga)}_2\text{O}_3$ grain (red line) clearly reveals the presence of the characteristic In $M_{4,5}$, and O K edges. In this case, the O K line shape is the characteristic of the $c\text{-In}_2\text{O}_3$ bixbyite cubic structure [62]. Meanwhile, the spectrum recorded from a Ga-rich area (green line) again shows the In $M_{4,5}$ line (less intense but confirming the presence of In^{3+}) but in this case the O K line profile coincides more closely with the previously reported $\beta\text{-Ga}_2\text{O}_3$

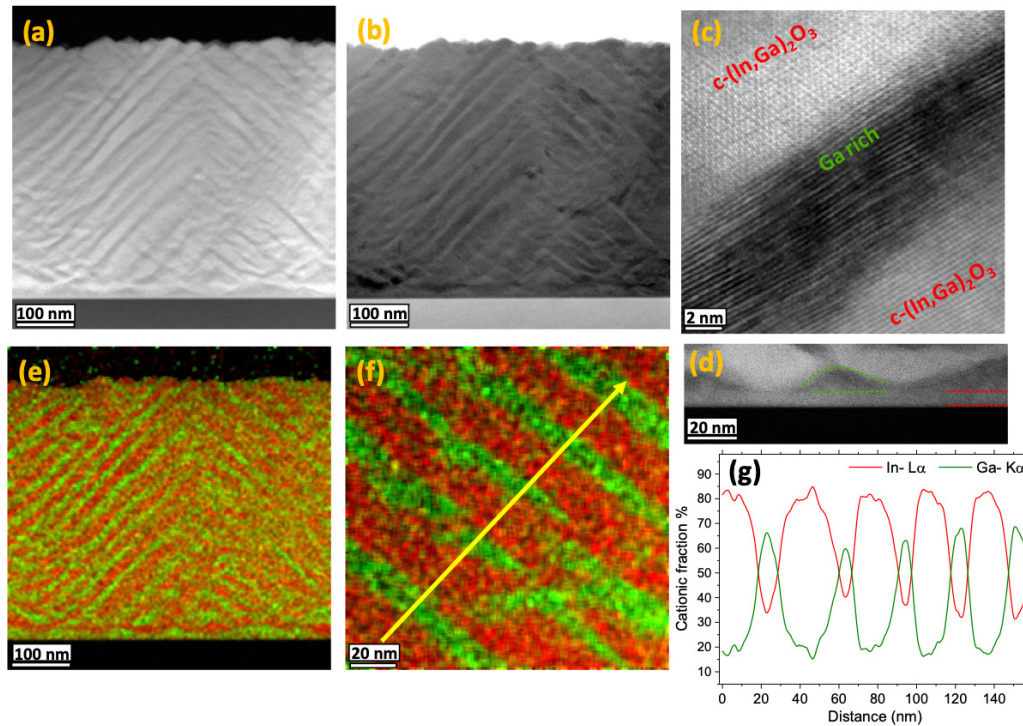


FIG. 8. STEM (a) HAADF and (b) BF images of the sample with $x = 0.35$. (c) Atomic resolution STEM HAADF. (d) High-magnification STEM HAADF of the area close to the substrate. (e) and (f) Corresponding STEM-EDXS maps for In $L\alpha$ (red) and Ga $K\alpha$ (green). (g) Cationic percentage for In $L\alpha$ (red) and Ga $K\alpha$ (green) across the yellow arrow marked in (f). The measured thickness of this sample is 450 nm.

polymorph [63]. The spectra corresponding to references $c\text{-In}_2\text{O}_3$ and $\beta\text{-Ga}_2\text{O}_3$ were also shown together for a better comparison. Variations can be observed in the ratio of the intensities of the two peaks forming the O K edge for Ga-rich regions and the reference $\beta\text{-Ga}_2\text{O}_3$. The high degree of substitution of Ga^{3+} by In^{3+} is likely to cause these differences [64]. Unfortunately, there is no EELS study in the literature for h-InGaO_3 to compare with, so the formation of this phase instead of the β -polymorph cannot be ruled out. In summary, increasing the Ga content to $x = 0.35$ causes segregation and the formation of Ga-rich regions, most likely small crystals of h-InGaO_3 with low crystallinity (not detectable by XRD).

V. CONCLUSIONS

Combinatorial pulsed laser deposition was used to prepare a $(\text{In, Ga})_2\text{O}_3$ material library with varying cation composition on r -plane sapphire substrates. XRD measurements indicate crystallization in the cubic bixbyite structure for the Ga content $x \leq 0.35$ with two, namely, the (111)- and the (110)-out-of-plane, orientations. The (111)-oriented crystals further exhibit two in-plane domains rotated by an angle of about 86.6° . The a -lattice constant and the absorption edge $E_{g,\text{opt}}$ systematically shift up to a Ga content of $x = 0.2$ at which both saturate. The lattice constant decreases and $E_{g,\text{opt}}$ increases linearly with x , respectively. Microstructural analysis of selected samples demonstrates a homogeneous incorporation of Ga_2O_3 into cubic In_2O_3 for $x = 0.11$. For $x = 0.22$, the cation distribution is no longer homogeneous and a segregation of Ga-rich and In-rich regions is observed. The sample with $x = 0.35$ is completely affected by this

segregation. Ga-rich regions exhibit a preferred orientation with an angle of $45^\circ\text{--}55^\circ$ with respect to the substrate normal, which has been shown to result from a correspondingly faceted In-rich bixbyite layer at the substrate–thin film interface. These Ga-rich regions likely have the hexagonal InGaO_3 crystal structure; however, crystallization in the monoclinic β -gallia structure cannot be ruled out. For $(\text{In, Ga})_2\text{O}_3$ grown by PLD on r -plane sapphire, a homogeneous alloying of Ga_2O_3 into cubic In_2O_3 was demonstrated up to $x = 0.20$, which enables tuning of the optical band gap between about 3.75 and 3.90 eV. Further studies are needed to identify the mechanism behind the observed segregation for $x > 0.22$ and possibly provide a means to adjust the ordering to obtain periodic arrangements that can be used, for example, in optical lattices and dielectric mirrors, anisotropic optical elements including filters and polarizers, graded index optics, metamaterials (negative index materials), Voigt wave propagation, and thus non-Hermitian optical systems with nontrivial topology and exceptional points.

ACKNOWLEDGMENTS

This study was supported by GraFOX, a Leibniz-Science Campus partially funded by the Leibniz Association. The Research Council of Norway is acknowledged for support to the Norwegian Center for Transmission Electron Microscopy (NORTEM; Grant No. 197405/F50) and the NANO2021 researcher project Functionalization of conducting oxides by ion beam and defect engineering (FUNCTION; Grant No. 287729). The authors would like to thank Chris Sturm and Lukas Trefflich for helpful discussions.

- [1] K. Kennedy, T. Stefansky, G. Davy, V. F. Zackay, and E. R. Parker, *J. Appl. Phys.* **36**, 3808 (1965).
- [2] N. C. Miller and G. A. Shirn, *Appl. Phys. Lett.* **10**, 86 (1967).
- [3] J. J. Hanak and J. I. Gittleman, *Phys. Lett.* **55**, 555 (1969).
- [4] H. Koinuma and I. Takeuchi, *Nat. Mater.* **3**, 429 (2004).
- [5] M. L. Green, I. Takeuchi, and J. R. Hatrick-Simpers, *J. Appl. Phys.* **113**, 231101 (2013).
- [6] H. von Wenckstern, Z. Zhang, F. Schmidt, J. Lenzner, H. Hochmuth, and M. Grundmann, *CrystEngComm* **15**, 10020 (2013).
- [7] M. Kneiß, P. Storm, G. Benndorf, M. Grundmann, and H. von Wenckstern, *ACS Comb. Sci.* **20**, 643 (2018).
- [8] H. von Wenckstern, M. Kneiß, A. Hassa, P. Storm, D. Splith, and M. Grundmann, *Phys. Status Solidi B* **257**, 1900626 (2019).
- [9] C. Fares, Z. Islam, A. Haque, M. Kneiß, H. von Wenckstern, M. Grundmann, M. Tadjer, F. Ren, and S. J. Pearton, *ECS J. Solid State Sci. Technol.* **8**, P751 (2019).
- [10] C. Fares, M. Kneiß, H. von Wenckstern, M. Grundmann, M. Tadjer, F. Ren, E. Lambers, and S. J. Pearton, *APL Mater.* **7**, 071115 (2019).
- [11] C. Fares, M. Kneiß, H. von Wenckstern, M. Grundmann, M. J. Tadjer, F. Ren, D. Hays, B. P. Gila, and S. J. Pearton, *ECS Trans.* **92**, 79 (2019).
- [12] C. Fares, M. Kneiß, H. von Wenckstern, M. Tadjer, F. Ren, E. Lambers, M. Grundmann, and S. J. Pearton, *ECS J. Solid State Sci. Technol.* **8**, P351 (2019).
- [13] C. Fares, M. Xian, D. J. Smith, M. R. McCartney, M. Kneiß, H. von Wenckstern, M. Grundmann, M. Tadjer, F. Ren, and S. J. Pearton, *J. Appl. Phys.* **127**, 105701 (2020).
- [14] A. Hassa, H. von Wenckstern, D. Splith, C. Sturm, M. Kneiß, V. Prozheeva, and M. Grundmann, *APL Mater.* **7**, 022525 (2019).
- [15] A. Hassa, H. von Wenckstern, L. Vines, and M. Grundmann, *ECS J. Solid State Sci. Technol.* **8**, Q3217 (2019).
- [16] A. Hassa, C. Wouters, M. Kneiß, D. Splith, C. Sturm, H. von Wenckstern, M. Albrecht, M. Lorenz, and M. Grundmann, *J. Phys. D* **53**, 485105 (2020).
- [17] A. Hassa, M. Grundmann, and H. von Wenckstern, *J. Phys. D* **54**, 223001 (2021).
- [18] A. Hassa, P. Storm, M. Kneiß, D. Splith, H. von Wenckstern, M. Lorenz, and M. Grundmann, *Phys. Status Solidi B* **258**, 2000394 (2021).
- [19] M. Kneiß, A. Hassa, D. Splith, C. Sturm, H. von Wenckstern, M. Lorenz, and M. Grundmann, *APL Mater.* **7**, 101102 (2019).
- [20] M. Kneiß, P. Storm, A. Hassa, D. Splith, H. von Wenckstern, M. Lorenz, and M. Grundmann, *Phys. Status Solidi B* **258**, 2000359 (2021).
- [21] C. Kranert, J. Lenzner, M. Jenderka, M. Lorenz, H. von Wenckstern, R. Schmidt-Grund, and M. Grundmann, *J. Appl. Phys.* **116**, 013505 (2014).
- [22] C. Kranert, M. Jenderka, J. Lenzner, M. Lorenz, H. von Wenckstern, R. Schmidt-Grund, and M. Grundmann, *J. Appl. Phys.* **117**, 125703 (2015).
- [23] V. Prozheeva, R. Hölldobler, H. von Wenckstern, M. Grundmann, and F. Tuomisto, *J. Appl. Phys.* **123**, 125705 (2018).
- [24] R. Schmidt-Grund, C. Kranert, T. Böntgen, H. von Wenckstern, H. Krauß, and M. Grundmann, *J. Appl. Phys.* **116**, 053510 (2014).
- [25] R. Schmidt-Grund, C. Kranert, H. von Wenckstern, V. Zviagin, M. Lorenz, and M. Grundmann, *J. Appl. Phys.* **117**, 165307 (2015).
- [26] P. Storm, M. Kneiß, A. Hassa, T. Schultz, D. Splith, H. von Wenckstern, N. Koch, M. Lorenz, and M. Grundmann, *APL Mater.* **7**, 111110 (2019).
- [27] J. E. N. Swallow, R. G. Palgrave, P. A. E. Murgatroyd, A. Regoutz, M. Lorenz, A. Hassa, M. Grundmann, H. von Wenckstern, J. B. Varley, and T. D. Veal, *ACS Appl. Mater. Interfaces* **13**, 2807 (2021).
- [28] H. von Wenckstern, D. Splith, M. Purfürst, Z. Zhang, C. Kranert, S. Müller, M. Lorenz, and M. Grundmann, *Semicond. Sci. Technol.* **30**, 024005 (2015).
- [29] H. von Wenckstern, D. Splith, A. Werner, S. Müller, M. Lorenz, and M. Grundmann, *ACS Comb. Sci.* **17**, 710 (2015).
- [30] X. Xia, C. Fares, F. Ren, A. Hassa, H. von Wenckstern, M. Grundmann, and S. J. Pearton, *ECS J. Solid State Sci. Technol.* **10**, 113007 (2021).
- [31] X. Xia, N. S. Al-Mamun, C. Fares, A. Haque, F. Ren, A. Hassa, H. von Wenckstern, M. Grundmann, and S. J. Pearton, *ECS J. Solid State Sci. Technol.* **11**, 025006 (2022).
- [32] Z. Zhang, H. von Wenckstern, J. Lenzner, M. Lorenz, and M. Grundmann, *Appl. Phys. Lett.* **108**, 123503 (2016).
- [33] S. I. Stepanov, V. I. Nikolaev, V. E. Bougrov, and A. E. Romanov, *Rev. Adv. Mater. Sci.* **44**, 63 (2016).
- [34] H. von Wenckstern, *Adv. Electron. Mater.* **3**, 1600350 (2017).
- [35] S. J. Pearton, F. Ren, M. Tadjer, and J. Kim, *J. Appl. Phys.* **124**, 220901 (2018).
- [36] A. J. Green, J. Speck, G. Xing, P. Moens, F. Allerstam, K. Gumaelius, T. Neyer, A. Arias-Purdue, V. Mehrotra, A. Kuramata, K. Sasaki, S. Watanabe, K. Koshi, J. Blevins, O. Bierwagen, S. Krishnamoorthy, K. Leedy, A. R. Arehart, A. T. Neal, S. Mou *et al.*, *APL Mater.* **10**, 029201 (2022).
- [37] H. Y. Playford, A. C. Hannon, E. R. Barney, and R. I. Walton, *Chem. Eur. J.* **19**, 2803 (2013).
- [38] K. L. Chopra, S. Major, and D. K. Pandya, *Thin Solid Films* **102**, 1 (1983).
- [39] H. von Wenckstern, D. Splith, S. Lanzinger, F. Schmidt, S. Müller, P. Schlupp, R. Karsthof, and M. Grundmann, *Adv. Electron. Mater.* **1**, 1400026 (2015).
- [40] H. von Wenckstern, D. Splith, F. Schmidt, M. Grundmann, O. Bierwagen, and J. S. Speck, *APL Mater.* **2**, 046104 (2014).
- [41] G. Korotcenkov, V. Brinzari, S. H. Han, and B. K. Cho, *Mater. Chem. Phys.* **175**, 188 (2016).
- [42] T. Addabbo, M. Bruzzi, A. Fort, M. Mugnaini, and V. Vignoli, *Sensors* **18**, 4410 (2018).
- [43] R. J. Cava, J. M. Phillips, J. Kwo, G. A. Thomas, R. B. v. Dover, S. A. Carter, J. J. Krajewski, W. F. Peck, J. H. Marshall, and D. H. Rapkine, *Appl. Phys. Lett.* **64**, 2071 (1994).
- [44] D. D. Edwards and T. O. Mason, *J. Am. Ceram. Soc.* **81**, 3285 (1998).
- [45] A. Regoutz, R. G. Egdell, D. J. Morgan, R. G. Palgrave, H. Tellez, S. J. Skinner, D. J. Payne, G. W. Watson, and D. O. Scanlon, *Appl. Surf. Sci.* **349**, 970 (2015).
- [46] F. Yang, J. Ma, C. Luan, and L. Kong, *Appl. Surf. Sci.* **255**, 4401 (2009).
- [47] L. Kong, J. Ma, F. Yang, C. Luan, and Z. Zhu, *J. Alloys Compd.* **499**, 75 (2010).
- [48] F. Zhang, K. Saito, T. Tanaka, M. Nishio, and Q. Guo, *Solid State Commun.* **186**, 28 (2014).

- [49] R. D. Shannon and C. T. Prewitt, *J. Inorg. Nucl. Chem.* **30**, 1389 (1968).
- [50] Z. Yang, W. Chen, S. Kuang, Z. Sheng, J. Shi, D. Chen, M. Cui, H. Qi, and K. H. L. Zhang, *Cryst. Growth Des.* **22**, 7325 (2022).
- [51] J. Feldl, M. Feneberg, A. Papadogianni, J. Lähnemann, T. Nagata, O. Bierwagen, R. Goldhahn, and M. Ramsteiner, *Appl. Phys. Lett.* **119**, 042101 (2021).
- [52] A. Papadogianni, C. Wouters, R. Schewski, J. Feldl, J. Lähnemann, T. Nagata, E. Kluth, M. Feneberg, R. Goldhahn, M. Ramsteiner, M. Albrecht, and O. Bierwagen, *Phys. Rev. Mater.* **6**, 033604 (2022).
- [53] Y. Seto and M. Ohtsuka, *J. Appl. Crystallogr.* **55**, 397 (2022).
- [54] F. Schmidt, D. Splith, S. Müller, H. von Wenckstern, and M. Grundmann, *Phys. Status Solidi B* **252**, 2304 (2015).
- [55] P. Vogt, A. Trampert, M. Ramsteiner, and O. Bierwagen, *Phys. Status Solidi A* **212**, 1433 (2015).
- [56] See Supplemental Material at <http://link.aps.org/supplemental/10.1103/PhysRevMaterials.7.094603> for additional experimental data.
- [57] H. Peelaers, D. Steiauf, J. B. Varley, A. Janotti, and C. G. Van de Walle, *Phys. Rev. B* **92**, 085206 (2015).
- [58] R. L. Weiher and R. P. Ley, *J. Appl. Phys.* **37**, 299 (1966).
- [59] M. Marezio, *Acta Crystallogr.* **20**, 723 (1966).
- [60] S. Geller, *Acta Crystallogr. A* **13**, 1023 (1960).
- [61] C. Wouters, C. Sutton, L. M. Ghiringhelli, T. Markurt, R. Schewski, A. Hassa, H. von Wenckstern, M. Grundmann, M. Scheffler, and M. Albrecht, *Phys. Rev. Mater.* **4**, 125001 (2020).
- [62] X. Liang and D. R. Clarke, *J. Appl. Phys.* **124**, 025101 (2018).
- [63] F. Tourtin, P. Armand, A. Ibanez, G. Tourillon, and E. Philippot, *Thin Solid Films* **322**, 85 (1998).
- [64] S. Roy, B. Malleshram, V. B. Zade, A. Martinez, V. Shutthanandan, S. Thevuthasan, and C. V. Ramana, *J. Phys. Chem. C* **122**, 27597 (2018).